

# Penetration of a transverse magnetic field by an accelerated field-reversed configuration

J. T. Slough and A. L. Hoffman

Redmond Plasma Physics Laboratory, University of Washington, Seattle, Washington 98102

(Received 23 June 1998; accepted 14 October 1998)

The field-reversed configuration (FRC) is a compact toroid with near unity  $\beta$  that is an ideal candidate to provide central fueling for large tokamaks. The study of the acceleration and penetration physics of the FRC into a transverse magnetic field gradient is necessary in order to evaluate the fueling efficiency of the FRC. To this end, experiments were conducted on the LSX/mod facility [J. T. Slough and A. L. Hoffman, *16th IAEA Fusion Energy Conference 1996* (International Atomic Energy Agency, Vienna, 1997), Vol. II, p. 237], where large mass (0.8 mg) FRCs were accelerated to high velocity ( $2 \times 10^5$  m/s), and then guided into a transverse magnetic field. Various diagnostics were employed to characterize the penetration process. These included thermocouple probes, magnetic probes, and emission arrays. A simple analytical model is developed that explains the basic features of the penetration process. Further modeling with two-dimensional numerical calculations provided for scaling laws to reach the conditions necessary to penetrate a large fusion tokamak. © 1999 American Institute of Physics. [S1070-664X(99)04701-1]

## I. INTRODUCTION

The direct fueling of the core of a fusion tokamak has several advantages. It leads to peaked plasma density profiles, which have been shown to increase the average fuel power density, and provides for an enhanced performance in tokamaks. Present fueling designs for the International Tokamak Engineering Reactor (ITER)<sup>1</sup> are pellet injection and gas puffing. Since neither scheme can penetrate the fusion plasma beyond the edge, fuel can only reach the plasma core by diffusive processes. A large portion of the fuel will thus be lost before burnup. Central fueling is essential to reduce the tritium inventory in the pumps and limiters. It could also play an important role in profile control for confinement, as well as a reduction in startup ionization losses, and may be essential for optimum ITER operation.

The design points for ignited operation in ITER call for operating either at or above the "Greenwald density limit."<sup>2</sup> The Greenwald density limit is an empirical limit, which has been found to describe the highest line-averaged density attainable in edge-fueled diverted tokamak discharges. It is given by  $n(10^{20} \text{ m}^{-3}) = I_p(\text{MA})/a^2(\text{m})$ . The density must be high in order to obtain sufficient power density for ignition and ultimately for viable reactor economics. In addition, the divertor scenarios chosen by ITER require high scrape-off layer (SOL) and divertor plasma densities in order to exhaust a large fraction of the alpha particle power by radiation and charge exchange. Density profiles obtained with the conventional fueling technique of gas puffing are predicted to be very flat in ITER, and this is well documented, for example, in the Joint European Torus (JET).<sup>3</sup> However, recent theoretical modeling suggests that the confinement quality of a reactor-grade tokamak discharge could be significantly enhanced if the density profiles could be peaked. If this theory were correct, density peaking would improve the ITER ignition margin substantially. Solid pellets, the cur-

rently envisioned fueling method, cannot be accelerated to the velocities necessary to penetrate far into an ITER scale plasma using the standard outside major radius launch techniques.<sup>4</sup>

Perkins *et al.*<sup>5</sup> examined the feasibility of accelerated compact toroids (CTs), for deep refueling of a large tokamak. A general rule derived for penetration is that the CT directed pressure,  $\rho v^2/2$ , be comparable to the tokamak central field pressure,  $B_{\text{tor}}^2/2\mu_0$ . Translated CTs have been produced experimentally as low- $\beta$ , oblate spheromaks<sup>6</sup> or high- $\beta$ , highly prolate, field-reversed configurations (FRCs).<sup>7</sup> Both CT configurations have been pursued as possible fuelers. The spheromak CT was the first to be employed for fueling a tokamak, and successful nondisruptive fueling has been demonstrated.<sup>8</sup> However, several factors limit the suitability of the spheromak as a fueler for ITER. The spheromak fuelers employ a magnetized Marshall gun that involves electrodes in the production of the plasma, and constant wall contact in the barrel of the injector. Impurity control is thus a major problem, and wall drag puts a severe limit on the acceleration efficiency (<5% for current injectors). The oblate nature of the spheromak combined with a low- $\beta$  formation limit, lead to large port requirements and extremely high rep rates due to the low mass load (10–60  $\mu\text{g}$  in the tokamak fueling experiments). These limitations can be avoided if refueling is accomplished using the FRC.

The FRC has been pursued for many years for its potential as a fusion plasma. Since the plasma is confined solely by poloidal fields, the equilibrium plasma  $\beta$  is typically quite high,  $\sim 0.9$ . The linear, cylindrical coil geometry allows for easy translation of the FRC from the formation chamber, and the electrodeless inductive formation produces plasmas with near unity  $Z_{\text{eff}}$ . The physics of the axial translation of FRCs into weaker magnetic fields has been studied in detail.<sup>5,9</sup> Experiments at this laboratory have extended these results by

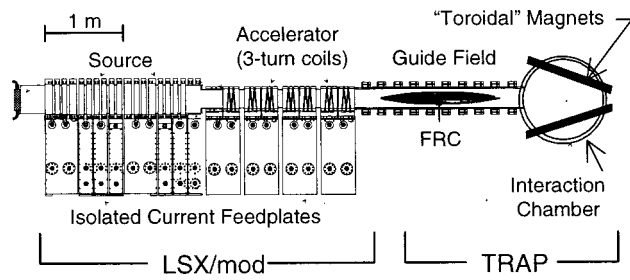


FIG. 1. Experimental layout of the LSX/mod source and TRAP magnets.

accelerating FRCs to directed velocities  $v_d \gg v_{thi}$ , the FRC ion thermal velocity.<sup>10</sup> The behavior of the FRC as it passes out of the confining axial field of the accelerator into the transverse toroidal field of the tokamak is the one unanswered question in the fueling process. To this end, the LSX facility was modified to include a smaller formation section and a four stage inductive accelerator (see Fig. 1). A guide field section and an interaction chamber with a transverse field was also added to complete the device that was used to study tokamak refueling by accelerated plasmoids (TRAP). Experiments were conducted to ascertain the behavior of the FRC as it passed into this field. The results of these experiments indicated that the behavior of the FRC could be explained as a simple one-dimensional analysis, where the effect of the transverse field could be reduced to that of a changing boundary pressure.

The paper is arranged as follows. A description of the TRAP experimental setup and associated diagnostics is given in Sec. II. Models of the interaction are developed in Sec. III. Two-dimensional (2-D) numerical calculations are presented that support the analytical model and allow for extension of the results to reactor-like regimes. Data from the interaction experiments are analyzed in Sec. IV. Comparisons to the analytical model, as well as 2-D numerical calculations, are examined. Section V contains conclusions and a discussion of the remaining unknowns in extrapolation to actual tokamak reactor refueling.

## II. EXPERIMENTAL SETUP

The overall layout of the LSX/mod-TRAP experimental apparatus is shown in Fig. 1. The primary component of LSX/mod is the 2.5 m long field-reversed theta pinch (FRTP) source. This section had several independently triggerable coils of constant radius ( $r_c = 0.23$  m) that were sequenced to initiate the acceleration process. Deuterium gas was puffed in from the upstream end of the source roughly 10 ms before initiating the source formation coils. This resulted in roughly a 20 mTorr fill pressure in the source section and negligible neutral gas pressure in the TRAP section. The fused silica vacuum wall decreased from 0.4 m diam in the source section to 0.27 m in the 2 m long acceleration section. In this region, the FRC was driven by (8) three-turn coils connected in (4) 0.5 m long groups. Details of the acceleration process will be given elsewhere.

After the acceleration section there followed a 2 m long transport section with a quasisteady solenoidal magnetic field

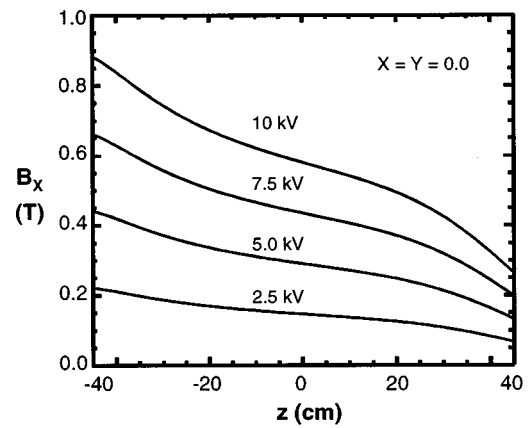


FIG. 2. Plot of the transverse magnetic field component  $B_x$  in the interaction chamber at  $X=Y=0$ .

designed to guide the FRC from the acceleration section into the transverse field chamber in the same manner that would be required in a large tokamak. Experimentally, this section was used to observe the FRC equilibrium prior to penetration. Finally, the TRAP experiment was equipped with a cylindrical stainless steel vacuum vessel where the axis of the cylinder was positioned in the up/down  $y$  direction. This orientation allowed for the maximum vacuum extent in the transverse  $x$  direction, and thus allowed the plasma flow in the transverse direction to be observed with the minimum wall interference.

The TRAP experiment utilized a pair of rectangular magnets on the end vacuum chamber to produce the transverse field. The magnets could be tilted to render a transverse field and field gradient similar to what would be found in a fully toroidal device. It was of sufficient size to simulate a tokamak with a major radius  $\sim 1.3$  m and an aspect ratio of 3.0. Due to stored energy limitations, the peak magnetic field was limited to less than 1.0 T in the interaction chamber (see Fig. 2). The interaction chamber ( $\sim 1$  m diam in the  $x$ - $z$  plane,  $\pm 0.3$  m in the vertical  $y$  direction) was large enough to observe the behavior of the FRC as it traveled from the axial field of the accelerator into the transverse field. The top surface of the interaction chamber was equipped with a large, 0.6 m diam fused silica window, which allowed plasma imaging and emission measurements of the interaction (see Fig. 3).

The toroidal magnets were multiturn and had a sufficiently long rise time ( $\sim 45$  ms) that the transverse field penetrated the stainless steel vacuum chamber as well as the transport magnets. The transport magnetic field was also formed by a set of pulsed multiturn coils, and was also slow enough ( $\tau_{1/4} \sim 2$  ms) to penetrate the interaction chamber walls and couple its flux into that of the transverse field. A plot of the magnetic field vectors for the joint interaction chamber field and transport field in the  $x$ - $z$  plane is shown in Fig. 4. It can be seen that the magnetic flux inside the transport coil maps into the toroidal field in the direction of the toroidal field. This has two consequences: the first is that plasma lost to the open field during acceleration continues on into the tokamak, where it is deposited on the outer flux

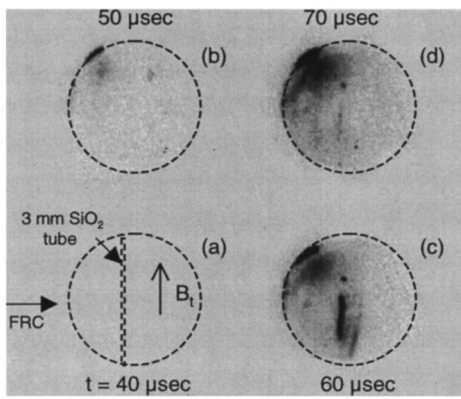


FIG. 3. Framing camera pictures of plasma emission during penetration into the transverse field corresponding to 7.5 kV. The camera was viewing from above along Y. Termination of the open field line plasma can be seen in all frames in the upper left corner on the interaction chamber wall. The FRC plasma, confined by internal fields, causes only the SiO<sub>2</sub> tube to glow only where it intercepts the FRC. The deflection of the FRC in the opposite direction to the open field flow can be observed in frame (c).

surfaces, thus avoiding plasma contact with the accelerator vacuum wall. The separation of unconfined open field line plasma from the FRC as it enters the interaction chamber can be seen in the framing pictures taken during FRC penetration (Fig. 3). The second consequence concerns the curvature of the transport flux as it exits the last guide field coil and merges into the transverse field. This bending creates a field gradient in the transverse *x* direction in the throat of the interaction chamber entrance. This additional field gradient imparts a sideways push to the FRC as it enters the interaction chamber. From Fig. 4, it can be seen that this push would be in the positive *x* direction, opposite the direction of the field. The deflection of the FRC in the opposite direction of the open field plasma can readily be seen in Fig. 3 (60 μs). This force caused the FRC to inject at an angle from normal with respect to the toroidal field (the angular displacement increasing with increasing transport field). In TRAP, the

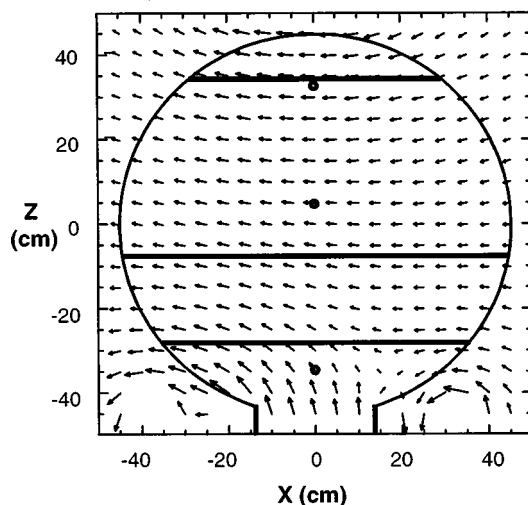


FIG. 4. The magnetic field vector plot in the *Y*=0 plane. The position of the interaction chamber and the various possible locations of the thermocouple SiO<sub>2</sub> tubes are also shown (circles indicate tubes in the *Y* direction).

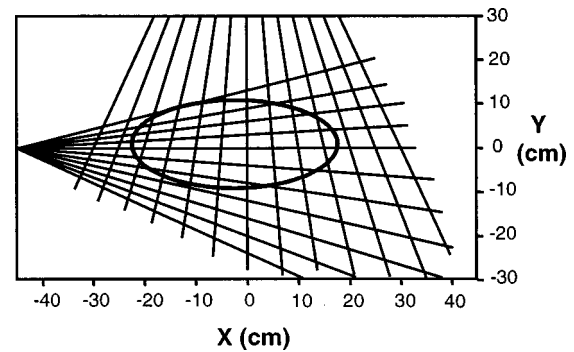


FIG. 5. The position of emission array chords in the *Z*=0 plane of the interaction chamber.

transverse deflection of the FRC was countered somewhat by image currents in the interaction chamber walls. This, however, caused the FRC to have, at times, a rather complex motion in the interaction field after injection.

The main diagnostics used to determine the FRC behavior in the interaction chamber were internal magnetic probes, pressure probes near the interaction chamber walls, collimated plasma visible emission arrays, and thermocouple probes. The latter two provided the clearest information regarding the behavior of the FRC and the FRC mass deposition.

The plasma emission arrays were positioned to view the FRC both up/down [ $\int \epsilon(y_i, z=0) dx$ ], and side to side [ $\int \epsilon(x_i, z=0) dy$ ] midway into the interaction chamber. An additional array, viewing vertically, was positioned along the axial direction as well [ $\int \epsilon(z_i, x=0) dy$ ]. The first two arrays monitored the FRC location up/down and side to side as it passed midway through the interaction chamber (see Fig. 5). The last array monitored the penetration of the FRC into the transverse field. The plasma emission in a band from 510 to 600 nm was found in previous FRC experiments<sup>11</sup> to be proportional to  $n^2$ . The filtered imaging diagnostics were thus quite useful in tracking the FRC mass density while discriminating against low-density background plasma. At various axial locations, as indicated in Fig. 4, small SiO<sub>2</sub> tubes (2 mm diam with 1 mm bore) were placed completely through the vacuum chamber in both *x* and *y* directions. The vacuum seal was made to the outside of the quartz tubes so that the bore was open to the atmosphere. During the discharge, the FRC translated over the tube, heating it. It was found from tubes placed between the accelerator and transport section, where the FRC size and directed energy are known, that the amount of tube heating was proportional to the plasma directed energy integrated over the FRC length. After the plasma discharge, these tubes would locally come into equilibrium at a higher-temperature proportional to the integrated energy deposited by the FRC. Due to the low thermal conductivity along the tube, the thermal imprint of the energy distribution would persist for several minutes. Immediately after a discharge, a small type E thermocouple was drawn through the tube at a rate that allowed for the thermocouple to be radiantly heated (or cooled) to the local tube temperature, which was then recorded.

### III. TRANSVERSE FIELD PENETRATION MODELS

#### A. One-dimensional adiabatic model

The description of the interaction of the FRC with a transverse field is, by its very nature, a three-dimensional problem. However, several simplifying assumptions and constraints can be made that render a description of the interaction process. The most important constraint is the constancy of the total energy inside the vacuum boundary of the tokamak-guide field system depicted in Fig. 4. It is assumed that there is no external energy added after the time the FRC enters the guide field from the acceleration coils with a directed velocity  $v_d$ . The total system energy inside this boundary,  $E_{tot}$ , consists of the tokamak magnetic field energy,  $E_{Bt}$ , the guide field vacuum magnetic energy,  $E_{Bgf}$ , the tokamak plasma energy,  $E_{pt}$ , the FRC internal plasma energy,  $U_p$ , the FRC internal magnetic energy,  $U_B$ , and the FRC directed energy  $1/2Mv_d^2$ , where  $M$  is the total FRC mass. It is further assumed that the time scale for penetration,  $\tau_{pen} \ll \tau_\phi, \tau_N, \tau_E$  the characteristic flux, particle, and thermal energy confinement times of the FRC, respectively. This implies that there is no exchange of energy between the FRC and the tokamak plasma prior to disassembly of the FRC at the end of penetration. Any expansion/compression of the FRC during penetration is thus an adiabatic one. The conservation of total energy allows one to relate the energy per unit mass of the FRC at a position  $z$  (or equivalently  $r$  in the toroidal field coordinates) in terms of the initial FRC conditions in the guide field, i.e.,

$$\frac{1}{2} v_d^2(z) + \hat{U}_p(z) + \hat{U}_{bt}(z) = \frac{1}{2} v_{d0}^2 + \frac{5}{2} \frac{NkT_0}{M}, \quad (1)$$

where  $T_0$  is the initial total FRC ion plus electron temperature. The second term on the right reflects that for a FRC in equilibrium with the axial guide field that the internal magnetic energy of the FRC,  $U_{Bgf} = NkT_0$ .<sup>12</sup> Here  $\bar{U}_p(z)$  is the normalized FRC plasma plus internal field energy when it is confined by the transverse field, and  $\bar{U}_{bt}(z)$  is the normalized change in transverse field energy due to the presence of the FRC. Any change in  $E_{pt}$  is assumed negligible.

If one further assumes that the ratio of internal magnetic to plasma energy is unaltered during penetration, one can rewrite Eq. (1) in the following form:

$$v_{d0}^2 - v_d(z)^2 = 5 \frac{N}{M} k [T(z) - T_0] = 5 \left( \frac{P}{\rho}(z) - \frac{P_0}{\rho_0} \right). \quad (2)$$

Assuming that the sideways motion due to the tilting force on the FRC is small, or equivalently  $\tau_{tilt} > \tau_{pen}$ , the body forces on the FRC can be ignored. The validity of this assumption will be discussed later.

It will also be assumed during penetration that within the FRC the ion density and temperature remain in a regime such that the collisionality is sufficiently large to assure that the ion-ion collision time,  $\tau_{ii} < \tau_{pen}$ , and also that  $\tau_{ii} < \tau_b$ , the ion axial transit time inside the FRC. With these assumptions, the FRC is in local pressure balance with the transverse field, and the following equation of state can be used:

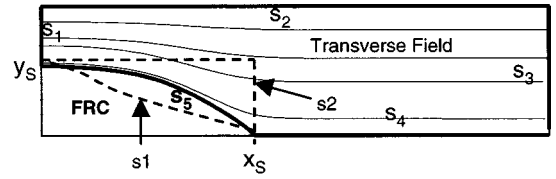


FIG. 6. Cross section of the FRC separatrix and the position of control surfaces in the transverse field.

$$\frac{P(z)}{P_0} = \left( \frac{\rho(z)}{\rho_0} \right)^\gamma. \quad (3)$$

Since the FRC compression/expansion is three-dimensional,  $\gamma = \frac{5}{3}$ . From Eqs. (2) and (3), one has

$$v(z)^2 = v_d^2 - 5 \frac{P_0}{\rho_0} \left[ \left( \frac{P(z)}{P_0} \right)^{2/5} - 1 \right]. \quad (4)$$

The magnetic pressure from the transverse field,  $P(z)$ , is assumed to be a scalar quantity that depends only on  $z$ . While this is intuitively obvious for the part of the FRC in the azimuthally symmetric axial guide field, it requires a bit of analysis to understand that it is also, at least approximately, correct in the transverse field as well. Consider the force per unit length on the FRC separatrix from the transverse field (see Fig. 6). Since  $\tau_\phi \gg \tau_p$ , the high conductivity of the FRC assures that screening currents keep the transverse field outside the FRC. The transverse field then wraps around the FRC, as shown in Fig. 6. The transverse field near the FRC at a given  $z$ ,  $B_t(z)$ , will be assumed to lie in the  $x$ - $y$  plane, where the coordinate  $x(y)$  is taken in the direction parallel (perpendicular) to the transverse field, as depicted in Fig. 6. The total force in the  $x$  and  $y$  direction on the FRC separatrix is obtained from an integration of the relevant component of the Maxwell stress tensor,

$$F_{x(y)}^i = \int (\hat{n}_i \cdot \vec{T})_{x(y)} dS_i, \quad (5)$$

where

$$(\hat{n}_i \cdot \vec{T})_{x(y)} = \frac{1}{\mu_0} (\hat{n}_i \cdot \vec{B}) B_{x(y)} - \frac{1}{2\mu_0} B^2 \hat{n}_i \cdot \hat{x}(\hat{y}). \quad (6)$$

For the FRC to be in force balance with the transverse field,

$$\sum_i^5 F_{x(y)} = 0. \quad (7)$$

Using Eq. (7), one can solve for the unknown force on the separatrix (surface  $S_5$  in Fig. 6) in terms of the four remaining terms. These terms can be easily evaluated for the force in the transverse field direction if one assumes that the vacuum wall is a flux-conserving boundary and is of constant height,  $y_w$ , at a given  $z$ . For a toroidal chamber with a metal wall, this would be a valid assumption on the fast time scale for penetration. One has, in this case, for the average force per unit length in  $z$ ,

$$F_x^s = \frac{B_t^2}{2\mu_0} \frac{y_s}{(1-\bar{y})}, \quad \bar{y} = \frac{y_s}{y_w}, \quad (8)$$

where  $B_t$  is the magnitude of the toroidal field in the absence of the FRC. If it is assumed that the FRC cross section is small compared to the tokamak height  $\bar{y} \sim 0$ , so that one has for the average pressure on the separatrix in the toroidal direction,

$$\langle P \rangle_x \cong \frac{B_t^2}{2\mu_0}. \quad (9)$$

Evaluation of the  $y$  component of force requires some knowledge concerning the separatrix shape. There are two limiting conditions that allow for a simple evaluation of the stress tensor integrals. These are depicted by dashed lines in Fig. 6. Shape 1 is such that at the wall there is a linear drop in the transverse field magnitude down to the vacuum value as  $x$  approaches  $x_s$ . Shape 2 maintains a constant value of  $B$  with a rapid transition to the vacuum value at  $x_s$ . The resultant forces in the  $y$  direction are

$$F_y^{S1(2)} = \frac{B_t^2}{2\mu_0} \frac{x_s}{(1-\bar{y})^{1(2)}}. \quad (10)$$

For case 1, where there is a linear drop in the field along the vacuum wall, the total force in the  $y$  direction is equal to that in the  $x$  direction. The FRC first enters the transverse field with a separatrix that is circular. It can be shown analytically that  $F_y = 2F_x$  for this case. More generally, it can be shown that for an elliptical FRC cross section  $F_y \cong (1 + 1/\sqrt{e})F_x$ , where  $e$  is the ellipticity. Thus there will be a rapid toroidal flow until a more elongated separatrix shape like case 1 is achieved. The final separatrix shape is a complicated function of the forces acting on the FRC surface currents required to exclude the transverse field, as well as the internal FRC currents. As long as the FRC responds adiabatically in maintaining force balance, the actual cross-sectional shape should not have a significant influence on the penetration.

The maximum penetration depth of the FRC into the transverse field is found by solving Eq. (4) for  $v(z) = 0$ . In the limit  $\bar{y} \ll 1$ , one has  $\langle P_x \rangle = \langle P_y \rangle = B_t^2/2\mu_0$ . In terms of the external axial guide field of the FRC before penetration,  $B_{gf}$ , one has

$$0 = v_{d0}^2 - \frac{5}{2} \frac{B_{gf}^2}{\mu_0 \rho_0} \left[ \left( \frac{B_t}{B_{gf}} \right)^{4/5} - 1 \right].$$

Solving for the transverse field at maximum penetration yields

$$B_t = B_{gf} \left( 1 + \frac{2}{5} K \right)^{5/4}, \quad (11)$$

where

$$K = \frac{\mu_0 \rho_0 v_{d0}^2}{B_{gf}^2} = \frac{\frac{1}{2} m_i v_{d0}^2}{kT}, \quad (12)$$

$$K^{1/2} = \frac{v_{d0}}{v_A} \equiv v_d^*.$$

Thus,  $K$  reflects the initial directed energy of the FRC ions in units of the plasma thermal energy. Here  $K^{1/2}$  can be seen to be the ratio of the initial FRC drift speed to the Alfvén speed

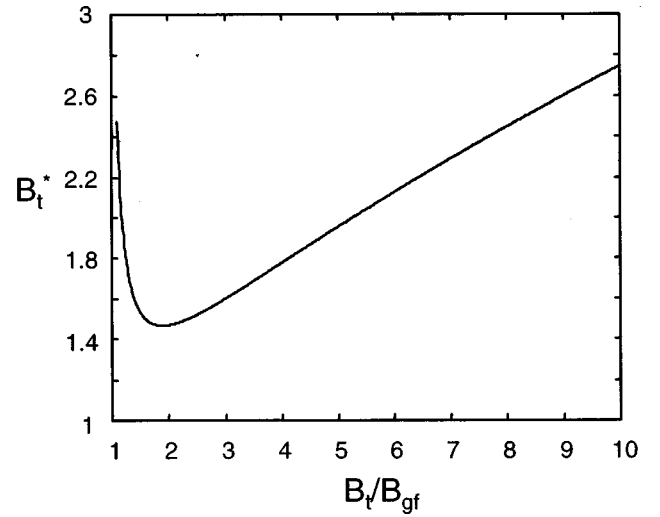


FIG. 7. Enhanced penetration factor  $B_t^*$  as a function of the maximum transverse magnetic field to the guide field ratio due to FRC compressibility.

in the guide field based on the FRC central density. This simple relationship holds due to the high- $\beta$  nature of the FRC.

The penetration depth for an incompressible conducting object (a copper bullet, for example) would be the point at which the magnetic pressure equals the kinetic energy density of the object or when  $B_t^2/\mu_0 = \rho v_d^2$ . This has typically been used as the criterion for the velocity for penetration into a field  $B_t$ . Due to the compression of the FRC in the transverse field gradient, there is deeper penetration for the same initial velocity. If one defines  $B_t^* = B_t/\sqrt{\mu_0 \rho_0 v_d}$ , one has, from Eq. (11),

$$B_t^* = \sqrt{\frac{2}{5}} \frac{B_t}{B_{gf}} \left[ \left( \frac{B_t}{B_{gf}} \right)^{4/5} - 1 \right]^{-1/2}. \quad (13)$$

A plot of  $B_t^*$  as a function of the field ratio  $B_t/B_{gf}$  is found in Fig. 7. The value of  $B_t^*$  is always greater than unity. Here  $B_t^*$  increases for field ratios that are larger and smaller than two. Large field ratios require the FRC to have a large directed energy compared to thermal i.e., large  $K$ . The increase in  $B_t^*$  for highly compressed FRCs ( $B_t/B_{gf} - 1$ ) is an unfavorable operating regime since the energy required to pre-compress both the FRC plasma and internal field is  $\sim \frac{5}{2} NkT$ , whereas the energy associated with increasing the drift speed  $\sim NkT$ .

## B. Numerical calculations

The conductivity and moment of inertia of the FRC are sufficiently large that for virtually any drift velocity  $v_d > v_{thi}$ , the time scale for penetration  $\tau_p \ll \tau_\phi, \tau_{fill}$ . To a good approximation, then, the FRC experiences the external transverse field mainly as a confining pressure at the separatrix. In this light, the behavior of the FRC during penetration can be modeled using a 2-D, fully resistive MHD code resolving the FRC dynamics in the  $r, z$  plane of the guide field. In this geometry, the gradient in field pressure experienced by the FRC in the  $y, z$  plane of the transverse field is produced by a conically shaped flux coil of the proper pitch and size, as

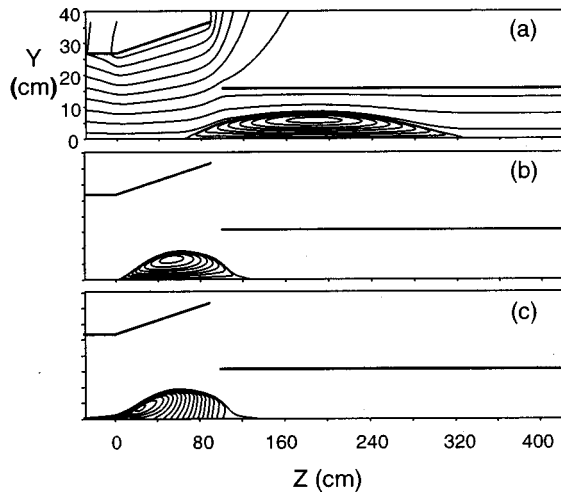


FIG. 8. (a) Flux contours prior to penetration. (b) FRC flux contours at maximum penetration ( $v_{\text{FRC}}=0$ ). (c) Density contours at maximum penetration.

sketched in Fig. 8. In this manner, even though the axial magnetic field does not change direction in the same manner at the transition from the guide to the transverse field, the field pressure experienced at the FRC separatrix is reproduced. Based on the force balance analysis, the FRC will behave in much the same way. The assumption of azimuthal symmetry in the 2-D calculations will not reproduce the FRC shape in the  $x$ - $y$  plane of the transverse field. In the interpretation of the 2-D results, then, the radial changes must be regarded as the average dimensional change of the FRC in this plane. Changes in the FRC cross-sectional area, however, should be preserved.

The range of applicability for the adiabatic 1-D model is resolved by the 2-D calculations. The FRC penetration process into a field pressure gradient similar to that employed experimentally is shown graphically in Fig. 8. Even though the FRC is far from equilibrium [ $p \neq p(\psi)$ ] during the penetration process, the FRC emerges after reflection with essentially the same velocity as initially. Nonisentropic processes such as shocks can occur during penetration and would convert the directed energy into thermal energy. The extent to which this occurs is indicated by the loss of directed energy in the calculations after FRC penetration and reflection. For a completely isentropic penetration, the directed velocity  $v_d$  of the FRC would change only in sign. Nonisentropic heating would be expected when the inward compression speed of the FRC approaches the local sound speed. This type of shock heating is readily observed during FRC formation when the external field is increased fast enough. High-density FRCs to a good approximation are isothermal with  $T_e = T_i$ . Due to the high- $\beta$  nature of the equilibrium, the sound speed in the FRC can be expressed as

$$v_s = \left( \frac{4}{3} \frac{P}{\rho} \right)^{1/2} \approx v_A. \quad (14)$$

The radial compression occurs over the distance the FRC travels in the transverse field. If  $R^*$  is defined as the ratio of the maximum penetration distance into the transverse field to

TABLE I. FRC base experimental conditions in guide field prior to penetration for source discharges at 20 Torr  $D_2$  fill pressure.

|  |                                     |
|--|-------------------------------------|
| External magnetic field, $B_{\text{gf}}$       | 0.61 T                              |
| Guide field flux conserving wall radius, $r_c$ | 0.16 m                              |
| FRC central number density, $n_0$              | $0.9 \times 10^{22} \text{ m}^{-3}$ |
| Central temperature, $T(T_e + T_i)$            | 100 eV                              |
| Separatrix radius, $r_s$                       | 0.08 m                              |
| Separatrix length, $l_s$                       | 1.5 m                               |
| FRC mass                                       | $6 \times 10^{-7} \text{ kg}$       |
| Directed velocity, $v_d$                       | $1.8 \times 10^5 \text{ m/s}$       |

the initial FRC separatrix radius in the guide field, one would expect significant nonisentropic heating to occur as  $v_d/R^* v_s \sim v_d^*/R^* \rightarrow 1$ . Several calculations were made for various interaction fields and FRC velocities and masses to better understand the effect of departure from the isentropic penetration predictions of Eq. (11). The experimental parameters given in Table I were used as the base condition in the 2-D calculations. The results of these calculations are given in Fig. 9. It was found that even when the penetration was essentially isentropic, the field that the FRC center of mass reached was less than that given by Eq. (11), with the deficit becoming greater with increasing  $v_d^*$ . The reason for this is seen most clearly at the higher values of  $v_d^*$ . The penetration depends on the mass density of the FRC. At high  $v_d^*$ , the deceleration of the front flux surfaces of the FRC results in a rapid flow of plasma along each flux surface to the front. The high  $\beta$  of the FRC means that there is little internal field pressure to retard this mass flow. There is then a very rapid decoupling between the FRC mass and flux. This behavior is readily observed in the experiments during FRC acceleration, but, of course, in the opposite direction. With most of the flux surface left behind, the FRC mass continues to penetrate at a much smaller cross section and higher density (see Fig. 10). The FRC plasma is magnetized so that the flux must eventually be pulled in as well. However, the mass density retained with the flux is now much lower than that required to penetrate into the higher field region of the high-density mass in front. The flux then acts like a parachute that eventually drags the FRC to a halt prior to maximum penetration.

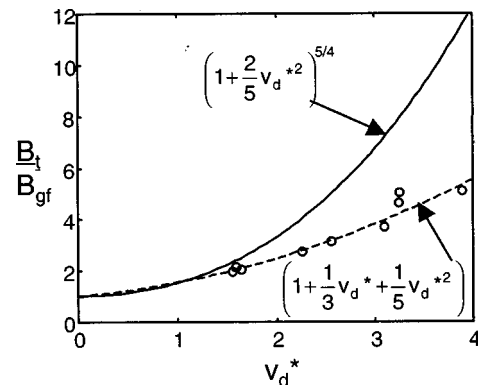


FIG. 9. The maximum transverse field to the initial guide field ratio as a function of the initial directed velocity normalized to  $v_A$ . The solid curve is given by an analytic adiabatic model. Circles represent numerical calculations with a dashed line as a fit.

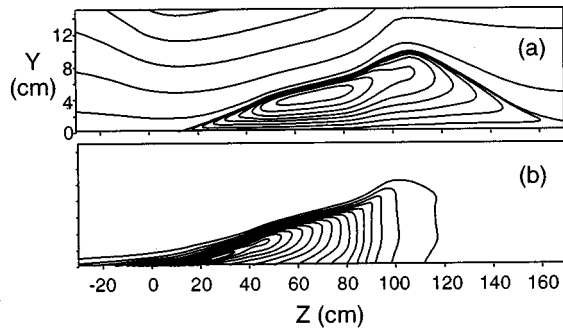


FIG. 10. Contours of (a) flux and (b) density for a FRC during penetration at high  $\nu_d^*$  ( $\sim 3$ ).

Calculations of the ratio of reflected to initial FRC velocity, which is a measure of the nonisentropic compression, are shown in Fig. 11. It is clear that the FRC penetration does become less isentropic as  $\nu_d^*/R^* \sim 1$ . This energy conversion appears to have little effect, however, on the penetration. Roughly, the same field is reached, regardless of how isentropic the penetration is [Fig. 11(b)]. That this is so indicates that the energy conversion is occurring at maximum inward compression, which occurs late in the penetration process.

**IV. EXPERIMENTAL RESULTS**

FRCs could be formed and accelerated over a wide range of conditions. However, due to the high-energy density of all FRCs formed, it was not possible to generate a transverse field with sufficient pressure to stop the FRC, even at the maximum coil voltage (see Fig. 2). Injecting the FRC with less velocity was not really an option, since the FRC acceleration process was not easily reversible. For example, although a large mirror field at the end of the guide field would momentarily slow the FRC as it passed, the FRC would regain the lost velocity as it was accelerated by the

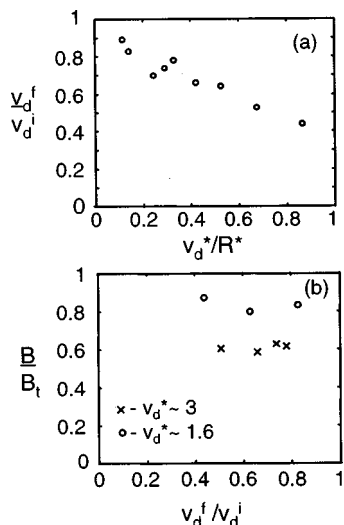


FIG. 11. (a) The ratio of FRC directed velocity before and after penetration is compared to the radial compression speed normalized to the sound speed ( $\nu_d^*/R^*$ ); (b)  $B/B_t$  is the ratio of the maximum field penetrated in the numerical calculations to that predicted by the analytic results.

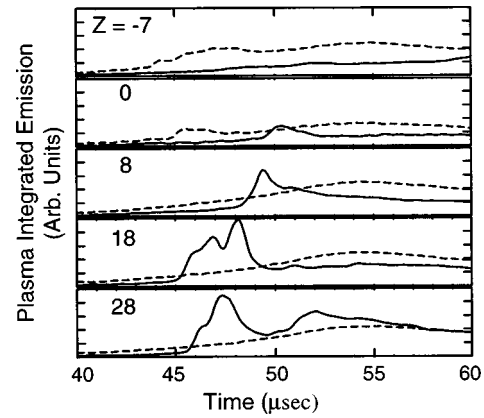


FIG. 12. Integrated plasma emission in y at various axial positions ( $x = 0$ ). The dashed line is data for the 10 kV interaction field and the solid line is at 2.5 kV (see Fig. 2).

mirror field gradient on exiting the mirror. Reducing the accelerator coil fields was not an option either. The subsequent slower passage of the FRC out of the transport throat region caused a strong interaction with the transport vacuum wall due to the side force in the transition region mentioned previously. The experimental procedure developed to understand the penetration process was to generate FRCs with the same density and velocity and to then vary the strength of the transverse magnetic field, and thus gradient field. The experimental conditions in the guide field are given in Table I. In this manner, the FRC position and cross section could be measured as the transverse field was increased. The observed values could then be compared to the numeric calculations.

At all transverse fields, it was found experimentally that the FRC, after traversing the interaction chamber, would be reflected by the conducting metal vacuum boundary of the interaction chamber far wall. Evidence of this can be readily found in the data from the axial emission array in Fig. 12. The plasma density was observed to rise rapidly at the emission array position farthest axially from the entrance (and thus nearest the back wall) of the interaction chamber. The density pile-up occurred because the magnetic flux inside the FRC could not penetrate the conducting wall boundary, and the FRC was reflected. The reflection from the wall was elastic enough to send the FRC mass back toward the entrance, as attested to by the appearance of the emission peak on progressively nearer emission array positions (see Fig. 12). At the highest fields, there was enough compression and slowing of the FRC by the toroidal field that the density wave was not observed. The emission data for the maximum toroidal field at 10 kV in Fig. 12 indicates that the FRC arrived at the back half of the interaction chamber at a higher density initially and remained fairly constant. For all cases, it was clear that the FRC was quite robust during penetration, with the internal field of the FRC providing confinement of the plasma throughout the interaction.

When the FRC contacted an insulating boundary (such as the fused silica vacuum or probe walls) immediate and intense light-up of the boundary would be observed, as hot plasma was allowed to come in contact with a cold boundary (see Fig. 13). After contact with  $\text{SiO}_2$ , impurities entrained

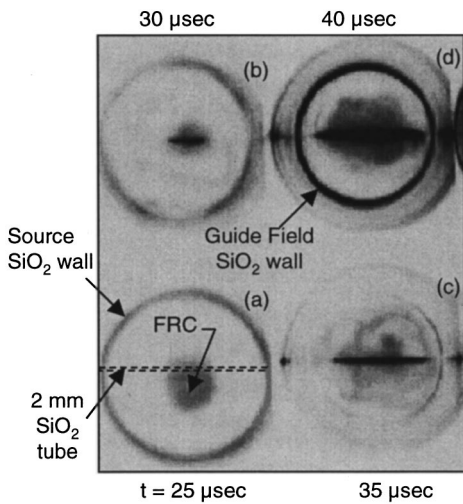


FIG. 13. End-on (viewing along Z from the source end) framing pictures of plasma emission as FRC traverses the SiO<sub>2</sub> tube positioned along a diameter between the acceleration and guide field coils (see Fig. 1). FRC is visible in frame (a) due to compression in the accelerator. The FRC becomes very bright in frame (d) due to heavy impurity pickup from the tube.

in the FRC would cause rapid cooling and decay of the FRC. The reflection from the metal boundary caused only minor plasma emission.

From the emission data, it was clear that the interaction with the conducting boundary resulted in a nonisentropic reflection. If the interaction were truly reversible, one would expect the FRC to eventually reappear in the axial guide field, which was not observed. It was possible to model the experimental behavior of the FRC in the experiment in the 2-D calculations by adding a coil that generated a strong magnetic field at the same axial position as the back wall of the interaction chamber. Due to the steep field gradient from this coil (large  $R^*$ ), the reflection off this “wall” in the

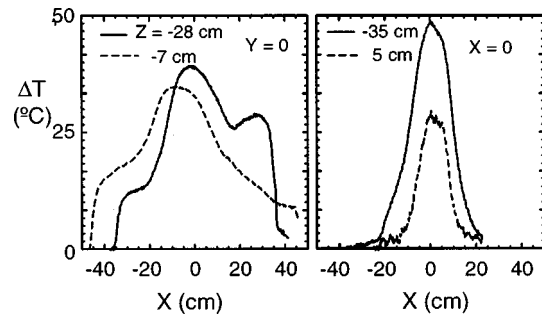


FIG. 15. Thermocouple temperature data for the interaction magnetic field corresponding to 7.5 kV. Solid lines indicate data for a discharge where the tubes were nearer the entrance of the interaction chamber.

calculation shown in Fig. 14 reproduced the nonisentropic reflection and area expansion observed experimentally. In the experiment, however, most of the expansion occurred in the transverse direction. The thermal conversion of directed energy accounts for this marked expansion of the FRC. This expansion can also be inferred from the thermocouple diagnostic data in Fig. 15. It can be seen that the FRC is well confined in the y direction perpendicular to the toroidal field, as might be expected. The further the FRC penetration the smaller becomes the FRC cross section in this dimension. The spread of the FRC in the toroidal x direction is also much less at a higher transverse field. There was a hot central heating of the silica tube that corresponded to visible emission from the first passage of the FRC across the tube. The much weaker heating in the wings of the tube right up to the chamber wall indicate the heating due to the large reflected FRC. Since the diagnostic is not time resolved, both heating patterns are superimposed on the tube.

The expansion of the FRC in the transverse direction is reduced significantly at higher fields. The FRC cross-

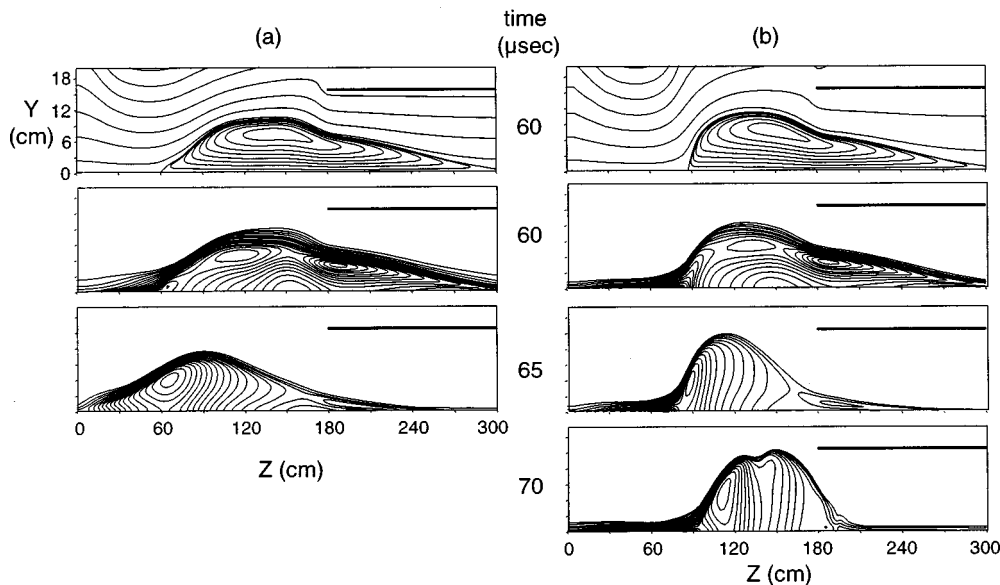


FIG. 14. Flux (top frames) and density contours (remaining frames) from numerical calculations for experimental conditions given in Table I. In time sequence (a) there is no end field sufficient to stop and reflect the FRC, while for (b) an additional field coil provides a steep field gradient sufficient for reflection as the metal wall does in the experiment. The radial swelling of the FRC can be seen after reflection.

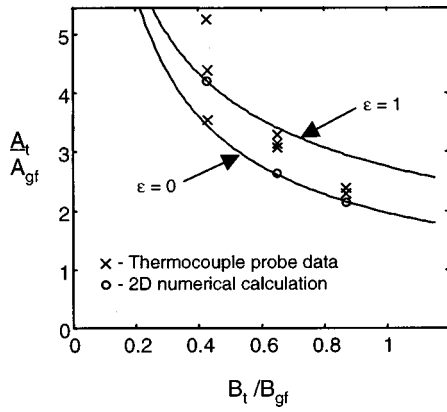


FIG. 16. Area of the FRC normalized to the Area of the FRC in the guide field for various ratios of the transverse to guide field. Here  $\epsilon=0$  corresponds to a FRC internal profile with the maximum flux, and  $\epsilon=1$  indicates the minimum flux.

sectional area, however, is the same as that observed in the 2-D numerical calculations under the same conditions (Fig. 16). Both the experiment and the calculations give area values that are consistent with simple scaling laws developed for reversible adiabatic FRC compression.<sup>13</sup> In the frame of the FRC, the passage out of the guide field into the transverse field chamber can be thought of as first a wall expansion into a larger flux conserver, followed by flux compression. Again, although the original analysis<sup>13</sup> considered the FRC to be in pressure balance with an axial field, as it was shown previously, the transverse field pressure at least yields the same average force on the FRC. Thus ignoring the FRC shape, the results should be very similar. As long as no walls are encountered, the penetration process is reversible, and it does not matter how the final state is reached. It will be assumed then that the wall expansion is done in a manner that leaves the ratio of FRC cross-sectional area to wall area unchanged. For this to be true, the intermediate transverse field,  $B'_t$ , after wall expansion is given by

$$B'_t = \frac{A_{gf}}{A_t} B_{gf}, \quad (15)$$

where  $A_{gf}$  and  $A_t$  are the guide field coil and transverse chamber wall cross-sectional areas. The transverse field is now increased to the final value observed with the wall area held constant. The scaling of the plasma area with external field pressure is, in general, dependent on the assumed internal pressure profile inside the FRC. The average  $\beta$  equilibrium constraint for FRC equilibria produces the following compressional scaling:<sup>13</sup>

$$\frac{B'_t}{B_t} = \left( \frac{A^f}{A'} \right)^{(3+\epsilon)/2}, \quad (16)$$

where  $A^f$  is the final FRC cross-sectional area and  $\epsilon$  is a constant where  $0 \leq \epsilon \leq 1$ , with the limits reflecting, respectively, the largest and smallest amount of flux possible for an equilibrium FRC. Virtually all experimentally measured profiles and numerically calculated equilibria yield a value of  $0 < \epsilon < 0.3$ . Remembering that the intermediate value of

$A'/A_t = A_0/A_{gf}$ , where  $A_0$  is the area of the FRC in the guide field, Eqs. (15) and (16) can be combined to give

$$\frac{A_f}{A_0} = \left( \frac{A_t}{A_{gf}} \right)^{(1+\epsilon)/(3+\epsilon)} \left( \frac{B_{gf}}{B_t} \right)^{2/(3+\epsilon)}. \quad (17)$$

The results of the experiment and the numerical calculations are in good agreement with the FRC area ratio predicted by Eq. (17) near the midpoint of the transverse field coil where the thermocouple data was taken. Both the experiment and the numerical calculations diverge somewhat from the model at a low field. The nonconstancy of the wall area as well as interference from the reflected FRC have a much larger effect on these much larger FRCs, and are thus contributing factors. The low-field results are not relevant to high-field penetration in any case.

The elongation of the FRCs in the transverse field inferred from both the thermocouple data and emission arrays is  $1.5 < e < 3$ . The magnitude of the tube heating from directed flow decreases with further penetration into the transverse field (Fig. 15). This decrease in directed energy is also found in the 2-D numerical calculations. From a comparison between calculations made with and without a "wall" coil, a significant part of the reduction in directed flow is due to backflow from the front of the FRC, which has been stagnated by reflection off the boundary wall.

It can also be seen in Fig. 15 that the position of the FRC has shifted  $\sim 10$  cm in the negative  $x$  direction caused by the sideways push in the throat region. It is possible to formulate an expression for the magnitude of the angle of deflection. The deflection arises from two sources. In the guide field, the deflection is caused by the reduction and increase of the axial guide field across the FRC due to the change of the axial component of the toroidal field (outward to inward) across the FRC. Outside the guide field coil, in the toroidal field edge region, this field difference diminishes rapidly due to the dipole nature of the guide field. The imparted force in the transverse (toroidal) direction is given by the difference in the magnetic pressure averaged over the FRC area normal to  $x$ . The resultant velocity,  $v_x$ , as a function of the distance traversed in the toroidal field of scale length  $L_{B_t}$  is

$$v_x(z) = \frac{1}{M} \int_{L_{B_t}}^z \frac{\Delta B_z^2}{2\mu_0} y_s l_s \frac{dl}{v_d}, \quad (18)$$

where  $\Delta B_z^2 = (\mathbf{B}_{gl} + \mathbf{B}_t)_z^2 - (\mathbf{B}_{gf} - \mathbf{B}_t)_z^2 = 4B_{gf}B_{tz}$ . In the guide field coil,  $B_{gz}(z) = B_{gf}$ , and one can approximate the magnitude of the  $z$  component of the toroidal field as  $B_{tz}(z) \approx B_t(l - z/L_{B_t})2x_s/L_{B_t}$ . It will be assumed that the FRC exits the guide field at the point where the toroidal field has dropped to one-third the central value,  $B_t$ . In the guide field, then, the  $v_x$  imparted to the FRC is

$$v_x(z) \cong \frac{4}{\pi} \frac{B_{gf}B_t}{\mu_0 \rho_0 L_{B_t} v_d} \int_z^{L_{B_t}} \left( 1 - \frac{z'}{L_{B_t}} \right) dz'. \quad (19)$$

The total displacement in the guide field,  $\Delta x_{gf}$ , if found from integrating  $v_x$  over the time the FRC, experiences the toroidal field influence in the guide field:

$$\Delta x_{\text{gf}} = \int_{L_{Bt}}^{\frac{2}{3}L_{Bt}} \nu_x(z) \frac{dz}{\nu_d} = \frac{4}{81\pi} \frac{B_t}{B_{\text{gf}}} \frac{L_{Bt}}{(\nu_d^*)^2}. \quad (20)$$

For the conditions of Table I and Fig. 15,  $\Delta x_{\text{gf}} \sim 2$  cm. The contribution to  $\nu_x$  in the toroidal field is analyzed in the same manner, but now  $B_{\text{gfz}}(z) \approx B_{\text{gf}}(l - z/R_{\text{gf}})$ , where  $R_{\text{gf}}$  is the guide field coil radius. Since this radius is typically small compared to  $L_{Bt}$ ,  $B_{\text{tz}}(z)$  can be considered constant at the guide field throat value of  $B_t/3$ . The resulting integrations yield

$$\Delta x_t = \frac{8}{3\pi} \frac{B_t}{B_{\text{gf}}} \frac{R_{\text{gf}}^2}{L_{Bt} \nu_d^{*2}}. \quad (21)$$

For the conditions referred to above,  $\Delta x_t \sim 2$  cm as well. Evaluating the terminal transverse velocity,  $\nu_{xf}$ , at the distance  $R_{\text{gf}}$  outside of the guide field coil, one has

$$\nu_{xf} = \left( \frac{1}{9} + \frac{R_{\text{gf}}}{L_{Bt}} \right) \frac{4}{\pi \nu_d^{*2}} \frac{B_t}{B_{\text{gf}}} \nu_d. \quad (22)$$

The final displacement at FRC stagnation, approximating the remaining penetration time as  $L_{Bt}/\nu_d$ , is then  $\Delta x_{\text{tot}} \approx \Delta x_{\text{gf}} + \Delta x_t + L_{Bt} \nu_{xf}/\nu_d$ . Evaluating this expression from Eqs. (20)–(22), it is clear that the last term is dominant. The terminal transverse velocity calculated for the FRC of Fig. 15 is  $1.8 \times 10^4$  m/s. The total displacement predicted at the thermocouple probe is 11 cm, which compares favorably with the measured deflection.

## V. CONCLUSIONS AND DISCUSSION

It has been found that an accelerated FRC can penetrate readily into a transverse magnetic field. The behavior of the FRC during penetration can be understood in terms of simple adiabatic scaling laws. It was seen that by considering the forces acting on the FRC during penetration, the analysis of the penetration could be modeled with a fully resistive 2-D numerical calculation. By modeling the experimental conditions, the numerical calculations reproduced the behavior of the FRC observed experimentally. Due to the relatively small influence of body forces during penetration (i.e., the torque on the FRC dipole moment) the numerical calculations were extended to examine FRC penetration into higher fields than could be achieved experimentally.

The penetration scaling from the analytical model predicts a very favorable scaling with increasing  $\nu_d^*$ , the initial penetration velocity normalized to the Alfvén speed in the guide field. The numerical calculations show a growing departure from the simple model at large values of  $\nu_d^*$  due to the differing dynamic behavior of the FRC mass and flux during penetration—a difference that is readily observed experimentally during FRC acceleration. The extrapolation required to achieve penetration into an ITER-scale toroidal field is not that large. An “empirically” derived scaling for the penetration field from the numerical calculations yields  $B_t/B_{\text{gf}} \approx 1 + \frac{1}{3}\nu_d^* + \frac{1}{5}\nu_d^{*2}$ . Using this formula, one can evaluate the conditions required for penetration into a 5 T core field of a fusion grade, tokamak reactor. With a guide field of 1 T, one has  $\nu_d^* = 3.7$ . Using the same fill pressure and

source size as used in the TRAP experiments, the required directed velocity  $\nu_d = 3.7 \times 10^5$  m/s, which is somewhat less than double that achieved in the TRAP experiments (max  $\nu_d \sim 2.1 \times 10^5$  m/s).

An unsolved problem is the disassembly of the FRC at maximum penetration. Clearly one does not want the FRC to be reflected as occurred in both experiment and modeling. Since the particle diffusion out of the FRC is too slow, the best disassembly mechanism will be reconnection of the FRC closed field with that of the tokamak toroidal field, which would directly empty the FRC mass. To enhance this reconnection process the FRC outer field should be anti-aligned with the toroidal field, thus allowing for rapid X point reconnection. This will naturally occur due to the tilting torque on the FRC. The torque  $\mathbf{T}$  from the transverse field acting on the FRC magnetic moment,  $m \approx \pi r_s^2 I_\theta$ , where  $I_\theta$  is the FRC toroidal current, is simply  $\mathbf{m} \times \mathbf{B}_t$ . Invoking the pressure balance with the external transverse field, the FRC poloidal field  $B_p \approx \mu_0 I_\theta / l_s = \sqrt{1 - \beta} B_t$ , with  $l_s$  the FRC length. The characteristic tilt time is given by  $\tau_{\text{tilt}} = \sqrt{\pi I_M / T}$ , where  $I_M$  is the moment of inertia of the FRC. Assuming a cylindrical FRC of mass  $M$ ,  $I_M = \frac{1}{4} M (r_s^2 + l_s^2/3)$ . Using these relations, one has then for the tilt time,

$$\tau_{\text{tilt}} = \left( r_s^2 + \frac{l_s^2}{3} \right)^{1/2} (\sqrt{1 - \beta})^{-1/4} \frac{1}{2\nu_A}, \quad (23)$$

where  $\nu_A$  is the Alfvén time based on the FRC central density and the external transverse field. For a typical FRC in TRAP,  $\beta \sim 0.9$  and  $l_s/r_s \sim 20$ . For adiabatic flux compression  $l_s \sim B_t^{-2/3}$ , and  $r_s \sim B_t^{-1/3}$ . However, even for a field compression ratio of 5, as assumed above, the length dependence of  $I_M$  is still the dominant term. One has then from Eq. (23) that  $\tau_{\text{tilt}} \approx l_s/\nu_A$ . Initially, with  $\nu_d^* > 1$ , the FRC would travel several FRC lengths before tilting, which justifies ignoring this torque in the analysis of the experiment. However, as the FRC slows at maximum penetration,  $l_s$  is also much shorter and the Alfvén speed higher. For isentropic compression,  $\nu_A \sim B^{2/5}$ , and one has then near maximum penetration  $\tau_{\text{tilt}}^f \approx \tau_{\text{tilt}}^i (B_{\text{gf}}/B_t)$ . The tilt time then becomes significantly shorter at the point in the FRC trajectory, where the FRC has the maximum dwell time. If the dwell time is defined as the time the FRC is within the inner one-third the tokamak minor radius  $r_t$ , one has  $\tau_{\text{dwell}} \approx (4/\sqrt{3})(r_t/\nu_{d0})$ . For a FRC whose initial length is roughly half the minor radius,  $\tau_{\text{tilt}}/\tau_{\text{dwell}} \sim (\sqrt{3}/8)(B_{\text{gf}}/B_t)\nu_d^*$ , and taking the penetration parameters discussed above, one has  $\tau_{\text{tilt}}/\tau_{\text{dwell}} \sim \frac{1}{6}$ , so that the anti-alignment of the FRC should easily occur during this time.

Reconnection at the X points must also occur during this time. If the steady reconnection models of Petschek and others<sup>14</sup> are assumed, the FRC lifetime  $\tau_{\text{FRC}} \sim 10(r_s/\nu_A)$ . For the parameters considered here, once the FRC has tilted, the disassembly time is no more than a few tilt times, and the disassembly of the FRC would also occur during the dwell time.

In conclusion, the robustness of the FRC in penetrating a transverse field has been demonstrated experimentally and modeled with a resultant scaling for penetration into higher

fields. Indications are that the parameters needed for penetration should allow for ample time for the FRC to tilt as well as be annihilated near the maximum field. However, to obtain further information concerning its usefulness as a fueler, experiments must be carried out on an actual tokamak.

## ACKNOWLEDGMENTS

The authors would like to thank P. A. Gurevich and Dr. R. D. Brooks for help in data reduction and analysis. The authors would also like to recognize K. E. Miller and M. Kostora for their contributions to the development and operation of the various diagnostics used in the experiments reported on here. The 2-D MHD numerical calculations carried out in this work were aided by many code improvements performed by Dr. Richard Milroy.

This work was sponsored by the U.S. Department of Energy.

- <sup>1</sup>R. Aymar, V. Chuyanov, M. Huguet *et al.*, *16th IAEA Fusion Energy Conference 1996* (International Atomic Energy Agency, Vienna, 1997), Vol. I, p. 3.
- <sup>2</sup>M. Greenwald, J. L. Terry, S. M. Wolf, S. Ejima, M. G. Bell, S. M. Kaye, and G. H. Neilson, *Nucl. Fusion* **28**, 2199 (1988).
- <sup>3</sup>The JET Team, *Nucl. Fusion* **32**, 187 (1992).
- <sup>4</sup>M. J. Gouge, K. D. St Onge, S. L. Milora, P. W. Fisher, and S. K. Combs, *Fusion Eng. Des.* **19**, 53 (1992).
- <sup>5</sup>L. J. Perkins, S. K. Ho, and J. H. Hammer, *Nucl. Fusion* **28**, 1365 (1988).
- <sup>6</sup>T. R. Jarboe, I. Hennins, H. W. Hoida, R. K. Linford, J. Marshall, D. A. Platts, and A. R. Sherwood, *Phys. Rev. Lett.* **45**, 1264 (1980).
- <sup>7</sup>D. J. Rej, W. T. Armstrong, R. E. Chrien, P. L. Klinger, R. K. Linford, K. F. McKenna, E. G. Sherwood, R. E. Siemon, M. Tuszewski, and R. D. Milroy, *Phys. Fluids* **29**, 852 (1986).
- <sup>8</sup>R. Raman, F. Martin, B. Quirion *et al.*, *Phys. Rev. Lett.* **73**, 3101 (1994).
- <sup>9</sup>H. Himura, S. Okada, S. Sugimoto, and S. Goto, *Phys. Plasmas* **2**, 191 (1995).
- <sup>10</sup>J. T. Slough and A. L. Hoffman, in Ref. 1, Vol. II, p. 237.
- <sup>11</sup>J. T. Slough and R. D. Milroy, *Rev. Sci. Instrum.* **61**, 3280 (1990).
- <sup>12</sup>M. Tanjyo, S. Okada, Y. Ito, M. Kako, S. Goto, T. Ishimura, and H. Ito, *Technol. Rep. Osaka Univ.* **34**, 201 (1984).
- <sup>13</sup>M. Tuszewski, *Nucl. Fusion* **28**, 2033 (1988).
- <sup>14</sup>H. E. Petschek, *AAS-NASA Symposium*, NASA SP-50, 425 (National Aeronautics and Space Administration, Washington DC, 1963).